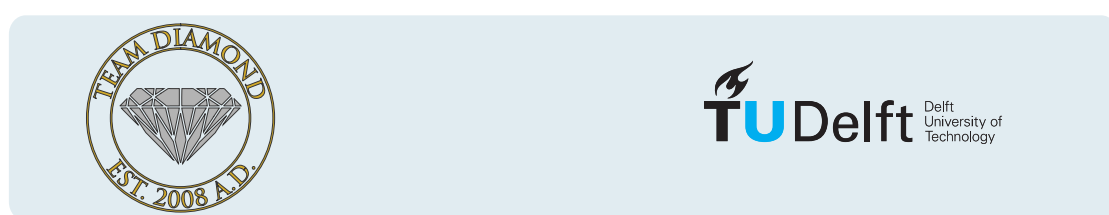


# Entanglement of Weakly-coupled Carbon-spins in Diamond

## MASTER OF SCIENCE THESIS

BY

Michiel Adriaan Rol



### *Supervisors:*

Ir. J.CRAMER,  
Dr. Ir. T.H.TAMINIAU,  
Prof. Dr. Ir. B. HANSON

*Performed at:*  
Quantum Transport group  
Kavli Institute of Nanoscience  
Faculty of Applied Sciences, TU Delft



## **Abstract**

Quantum error correction (QEC) is an essential ingredient for scaling up a quantum computer. The nitrogen-vacancy (NV) center in diamond is a promising candidate for such a scalable quantum computer. This thesis will first explain the tools available to control the NV-center and strongly coupled spins in its environment. We will then demonstrate how the spin register can be extended by addressing weakly coupled carbon-spins. The main result of this thesis is the creation of entanglement between two weakly coupled spins, for which initialization, control and read-out is required. We demonstrate entanglement with a fidelity of  $F = 0.76 \pm 0.02$ , well above the quantum limit for an entangled state. The last chapter will provide an outlook on how the capabilities developed can be extended to implement QEC.



# Contents

<b>1</b>	<b>Introduction</b>	<b>5</b>
1.1	Quantum Computing . . . . .	5
1.2	Quantum Error Correction . . . . .	5
1.3	The Nitrogen Vacancy Center in Diamond . . . . .	6
1.4	Goal of the project . . . . .	6
<b>2</b>	<b>The Nitrogen-Vacancy center in Diamond</b>	<b>7</b>
2.1	The electronic spin . . . . .	7
2.1.1	Initialization and readout of the electronic-spin state . . . . .	7
2.1.2	Controlling the electronic-spin state . . . . .	8
2.2	Controlling nuclear spins . . . . .	8
2.2.1	The Hyperfine Interaction . . . . .	8
2.2.2	Controlling the nitrogen nuclear spin . . . . .	9
2.2.3	Hyperfine coupling of carbon-13 spins . . . . .	9
2.2.4	Strongly coupled spins . . . . .	10
2.3	Decoherence . . . . .	10
2.3.1	Decoherence time . . . . .	10
2.3.2	Relation between decoherence and transition broadening . . . . .	11
<b>3</b>	<b>Addressing Weakly-coupled Carbon Spins</b>	<b>13</b>
3.1	Extending Electron Coherence . . . . .	14
3.1.1	Spin-Echo . . . . .	14
3.1.2	Dynamical Decoupling . . . . .	14
3.1.3	Dynamical decoupling spectroscopy . . . . .	14
3.2	Identifying weakly-coupled carbon-spins . . . . .	15
3.2.1	The effect of dynamical decoupling on nuclear spins . . . . .	15
3.2.2	Identifying Individual Carbon-spins . . . . .	17
3.3	Characterizing weakly-coupled carbon spins . . . . .	17
3.3.1	Basic operations . . . . .	17
3.3.2	Carbon Ramsey experiment . . . . .	18
<b>4</b>	<b>Entangling Weakly-coupled Carbon Spins</b>	<b>21</b>
4.1	Initialization and readout of single spins . . . . .	21
4.2	Parity measurements . . . . .	22
4.3	Quantum state tomography . . . . .	23
4.3.1	Readout . . . . .	23
4.3.2	Initialization and tomography of multiple weakly coupled spins . . . . .	23
4.4	Demonstrating entanglement between weakly coupled carbons . . . . .	23

<b>5 Towards Quantum Error Correction</b>	<b>27</b>
5.1 Deterministic Parity Measurements . . . . .	27
5.2 Multi Qubit Control . . . . .	27
5.2.1 Working of the simulations . . . . .	27
5.2.2 Results of the simulation . . . . .	28
<b>A Dynamical Decoupling Spectroscopy</b>	<b>35</b>
A.1 Mathematical description of dynamical decoupling spectroscopy . . . . .	35
A.2 Fingerprint analysis . . . . .	35
<b>B Constants and Experimental values</b>	<b>37</b>

## Introduction

### 1.1 Quantum Computing

The idea of using a quantum mechanical system to simulate physics was first explored by Feynman[9]. Because the number of operations required to simulate a quantum system scales exponentially with the number of particles in the system it is not feasible to classically simulate such a system. By manipulating a quantum mechanical system directly this scaling problem can be circumvented.

It was the idea of quantum simulation that led to the idea of exploiting quantum effects to perform computations. Shor's algorithm [23] is a prime example of how the advantageous scaling of quantum systems can be exploited to perform more efficient computations.

Shor's algorithm is an algorithm for prime factorization, where the best known classical algorithms for prime factorization scale exponentially Shor's algorithm scales polynomially. Because of the speedup provided by Shor's and other quantum algorithms it is possible to solve classes of problems that were previously unsolvable, such as the breaking of RSA encryption that relies on prime factorization being a computationally hard problem. Shor's algorithm has been shown to work on a small scale quantum computer [28]. However to take full advantage of the efficient scaling behaviour of quantum computations a scalable quantum computer is required.

### 1.2 Quantum Error Correction

One of the main challenges in creating a scalable quantum computer is the effect of errors. Because a quantum computer uses entanglement between multiple qubits as a resource an error on a single qubit can quickly propagate through the system. Using quantum error correction (QEC) it is possible to correct for such errors. The threshold theorem states the final error probability of a quantum algorithm on a large register can be made arbitrarily small, if the probability of an error on a single qubit is below a certain threshold and QEC is applied [15]. This makes quantum error correction a stepping stone on the way to realizing a scalable quantum computer [17].

Experiments demonstrating a form of QEC have been demonstrated in a range of systems. Codes correcting for one type of quantum error have been implemented with nuclear magnetic resonance [5, 16], trapped ions [22] and superconducting qubits [19]. Recently two groups have implemented three qubit gate based QEC using the nitrogen-vacancy (NV) center in diamond [26, 29].

Although schemes exist to implement a scalable quantum computer using a purely gate based architecture most approaches rely on correcting for quantum errors by performing repeated parity measurements. An example of such an approach is surface coding [10]. For this reason the present work will focus on performing the parity measurements required for such error correcting schemes.

QEC is similar to classical error correction through majority voting. In classical majority voting a single bit is encoded onto a *logical* bit consisting of multiple regular bits. When an error on a bit has occurred the original bit can be recovered by measuring all the individual bits and determining the original state by majority voting.

In QEC the quantum bit (qubit) is encoded onto a logical qubit consisting of multiple regular qubits. A consequence of classical majority voting is that it destroys a quantum state because it requires all bits to be measured. By measuring the parity of two qubits the difference between two states can be determined without measuring the individual states. If two states are parallel in the parity basis the parity measurement will return a positive result, if they are anti-parallel a

negative result. Performing a parity measurement on multiple qubits allows quantum errors, such as a bit-flip, a phase-flip or the combination of both, to be diagnosed.

Figure 1.1 shows a circuit diagram for three qubit measurement based QEC. The state  $|\psi\rangle_{C2}$  is encoded onto a logical qubit consisting of qubits C1, C2 and C3. A parity measurement is performed on qubits C1 and C2, and on C2 and C3, by reading out an ancilla qubit e. From the result of the parity measurements it can be determined on which qubit an error occurred.

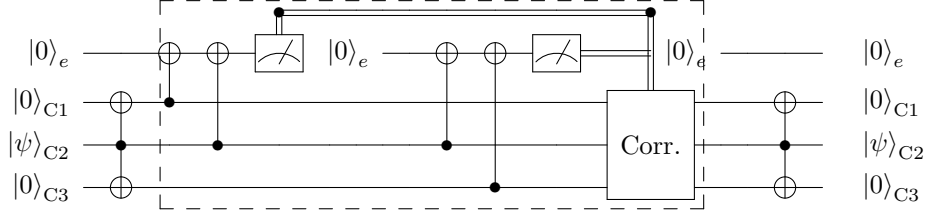


**Figure 1.1** – Gate circuit for three qubit error correction. First the state of  $C2$  is encoded onto three qubits. To diagnose an error an ancilla qubit is used to perform two parity measurements on the encoded qubits. The result of these measurements is used to determine what gates to apply to correct for the error if it occurred. These error correcting operations (in the dashed lines) can be repeated to continuously protect the encoded qubits against quantum errors. The three qubit error correction code can correct for one type of quantum error.

In order to implement measurement based error correction as depicted in Fig. 1.1 we require control over three qubits and an ancilla that can be read out. Furthermore we need to be able to perform parity measurements on these qubits and deterministically perform operations based on the outcome of these parity measurements to correct for errors.

### 1.3 The Nitrogen Vacancy Center in Diamond

Optical links [3, 18] Nodes [26, 29] (error correction)

Prominent approach to Scalable networks rely on repeated parity measurements (i.e. approach surface code. )

The Nitrogen Vacancy centre in diamond is a well investigated system[8] and a promising candidate for quantum computation[4]. In order to implement three qubit measurement based QEC we need three qubits plus ancillae that we can initialise, measure and conditionally perform operations on. These extra qubits are found in Carbon–13 atoms, which are normally a source of decoherence. These atoms can be addressed using a resonant decoupling sequence[25].

### 1.4 Goal of the project

The Goal of the project is to create entanglement between weakly coupled carbon spins. This is important because entanglement creation is a key component for QEC in particular and QI in general.

For this we need a b and c

# 2

## The Nitrogen-Vacancy center in Diamond

The nitrogen-vacancy (NV) center in diamond provides a natural occurring qubit register in a solid state environment. This chapter will explain how the electronic and nuclear spins can be initialized, controlled and read-out using optical and microwave pulses.

The methods described in this chapter are limited to nuclear spins for which spin transitions can be addressed selectively. The addressing of spins for which the spin transitions cannot be readily resolved will be discussed in Chapter 3.

### 2.1 The electronic spin

The NV-center is a naturally occurring impurity in diamond consisting of a substitutional nitrogen and an adjacent lattice vacancy (Fig. 2.1a). The NV-center can be in a neutral charge state ( $\text{NV}^0$ ) or in a negatively charged state ( $\text{NV}^-$ ). In this thesis we are mainly interested in the negatively charged state, where an additional electron is captured from the environment. For the  $\text{NV}^-$  the ground state is a spin-triplet that forms the basis of our qubit.

The electronic ground state can be described by the Hamiltonian [2]:

$$H_{\text{GS}} = \Delta S_z^2 + \gamma_e \mathbf{B} \cdot \mathbf{S} \quad (2.1)$$

Where  $\mathbf{S}_i$  are the Pauli-spin operators,  $\gamma_e = 2.802 \text{ MHz/G}$  the electron gyro-magnetic ratio and  $\Delta \approx 2.88 \text{ GHz}$  the zero-field splitting. In this expression the interactions with the nitrogen nucleus and the carbon spin bath are not included. In the experiments a magnetic field  $B_z = 304 \text{ G}$  is applied along the NV-axis<sup>1</sup>. The magnetic field lifts the degeneracy of the  $m_s = \pm 1$ .

In this thesis we define our electronic qubit as the two level system  $m_s = 0 := |0\rangle$  and  $m_s = +1 := |1\rangle$ .

#### 2.1.1 Initialization and readout of the electronic-spin state

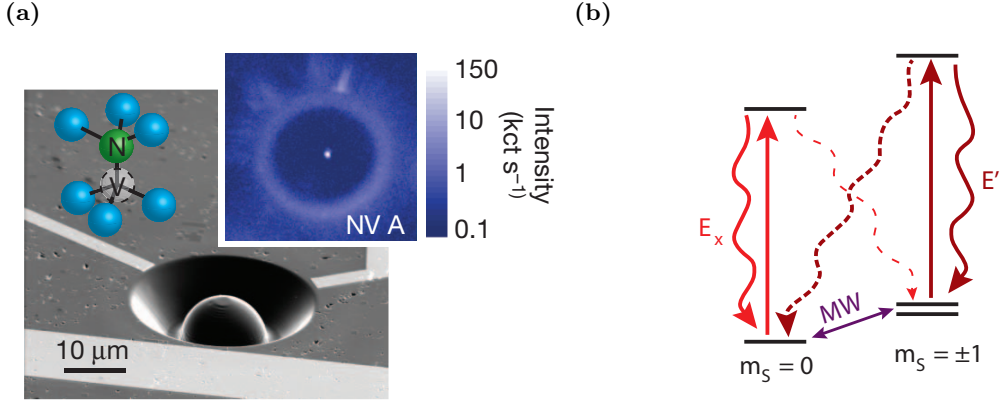
The transitions between the electronic ground-state and excited state are spin dependent and lie in the optical domain ( $\sim 637 \text{ nm}$ ). At low temperatures these transitions can be resonantly excited. For this reason, experiments were performed at cryogenic temperatures (4 K). The exact frequencies of these transitions depend on magnetic field and strain [13].

Figure 2.1b shows the optical transitions used to initialize and read-out the electronic spin. The  $E'$  transition excites both the  $m_s = +1$  and the  $m_s = -1$  states to the excited state. The  $E_x$  transition excites the  $m_s = 0$  state to the excited state. There is a small probability that the spin is flipped in an optical cycle, denoted by the dashed line.

By cycling an optical transition the spin state can be read-out and initialized [21]. By applying a pulse to the  $E_x$  transition a photon can be detected when the state falls back to the ground state. Because the  $E_x$  only excites the  $m_s = 0$  state photons can only be detected when the system is in the  $|0\rangle$ -state.

By pumping one of these transitions the spin can be initialized. Pumping will cause the population to cycle between the ground and excited state with a small probability of the spin flipping. When the spin flips it ends up in the state that is not being excited and stays there.

<sup>1</sup>The NV-axis is the axis going through both the nitrogen and the vacancy.



**Figure 2.1** – (a) Scanning electron microscope image of a solid immersion lens (SIL) similar to those used in the experiments. Overlaid sketch shows a schematic representation of the NV-center. Inset shows a confocal microscope image of an NV-center similar to those used in the experiments. Figure from Robledo et al. [21]. (b), Energy levels used for initialization and readout of the electronic-spin state. Figure from Robledo et al. [21]

Because the number of pumping cycles before the spin flips is limited, the fidelity with which the spin can be read-out is limited by the detection efficiency of the emitted photons. A solid immersion lens (SIL), visible in Fig. 2.1a, is milled onto the sample to maximize the detection efficiency.

Using these methods a readout fidelity of  $F = 90.55 \pm 0.40\%$  can be reached.

### 2.1.2 Controlling the electronic-spin state

The state of a qubit can be represented as a vector on the Bloch-sphere where the  $|0\rangle$ -state lies at the north pole and the  $|1\rangle$ -state at the south pole. The state vector rotates around the quantization-axis with a frequency depending on the energy splitting between the two states: the Larmor frequency. For the NV-electronic spin the quantization axis points in the z-direction (towards  $|0\rangle$ ) and the Larmor frequency is given by Eq. (2.2):

$$\omega_L = \Delta + \gamma_e B_z \quad (2.2)$$

By applying an external field a term is added to the Hamiltonian, the quantization-axis is changed, thereby changing its evolution. By applying microwaves with a frequency equal to  $\omega_L$  the transition between  $|0\rangle$  and  $|1\rangle$  can be driven [14]. Resonant microwave pulses are applied to the sample through an on-chip gold stripline, visible in Fig. 2.1a as the light area just below the SIL.

## 2.2 Controlling nuclear spins

The electronic-spin interacts with each nuclear spins in its environment through the hyperfine interaction, which is dependent on their position. Dependent on the strength of the hyperfine interaction close by spins can be controlled directly by applying microwave pulses.

### 2.2.1 The Hyperfine Interaction

The coupling between the electronic spin of the NV-center and a nuclear-spin is given by the hyperfine-interaction. The hyperfine interaction is a spin-spin interaction.

For nuclear spins the Hamiltonian therefore depends on the electronic spin-state of the NV-center. For a magnetic field ( $B_z$ ) in the z-direction the Hamiltonian is given by Eqs. (2.3) and (2.4) [26]:

$$H_0 = -QI_z^2 + \gamma_n B_z I_z \quad (2.3)$$

$$H_1 = -QI_z^2 + \gamma_n B_z I_z + H_{HF} \quad (2.4)$$

Corresponding respectively to the electronic spin being in the  $m_s = 0$  and in the  $m_s = \pm 1$  state. Where  $I$  and  $S$  are the nuclear and electronic spin operators,  $\gamma_n$  is the gyro-magnetic ratio of the nucleus and  $Q$  is the nuclear quadrupole splitting. The quadrupole term is  $Q = 2\pi \cdot 4.946$  MHz for the nitrogen spin [2]. The quadrupole term is not present for carbon-13 spins.

The Larmor frequency for a nucleus is given by Eq. (2.5):

$$\omega_L = -QI_z^2 + \gamma_n B_z \quad (2.5)$$

### 2.2.2 Controlling the nitrogen nuclear spin

The nitrogen-spin adjacent to the vacancy can be controlled using the hyperfine interaction. Because both the zero-field splitting  $\Delta$  of the electronic-spin is much larger than the hyperfine coupling between the nuclear and electronic spin ( $A_N = 2\pi \cdot 2.186$  MHz), the secular approximation can be used, leading to the following system Hamiltonian:

$$H_{GS} = \Delta S_z^2 + \gamma_e \mathbf{B} \cdot \mathbf{S} - QI_z^2 + \gamma_n B_z I_z - A_N S_z \cdot I_z \quad (2.6)$$

The hyperfine interaction between the nitrogen and electronic spin causes the transition between  $m_s = 0$  and  $m_s = 1$  to be split. This magnitude of the splitting is equal to  $A_N$  and is clearly resolved in the Electron Spin Resonance (ESR) shown in the top panel of Fig. 2.2.

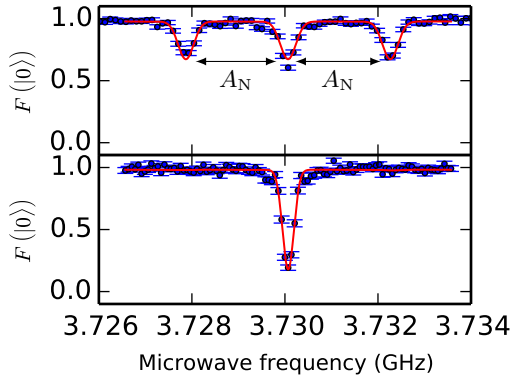


**Figure 2.2** – Electron Spin Resonance (ESR) for uninitialized (top) and initialized nitrogen spin (bottom) of the  $m_s = 0 \rightarrow m_s = +1$  transition. In the ESR the spin is prepared in  $|0\rangle$ , a microwave pulse is applied and the electron is read out. The microwave frequency is swept. When the microwave is on resonance the spin will be rotated out of  $|0\rangle$  and a decrease will be visible in the signal. In the top figure the transition is split due to the interaction with the NV's nitrogen nuclear spin. In the lower figure the nitrogen spin state is initialized and the splitting disappears.

The hyperfine interaction can be used to measure the nitrogen's spin state. Every time an experiment is started the nitrogen starts out in a mixed state. This means that every time an uninitialized nitrogen is measured it is equally likely to end up in one of its three states, as can be seen in the top panel of Fig. 2.2. The nitrogen state can be measured by initializing the electron in the split  $m_s = +1$  state and driving one of the transitions to  $m_s = 0$ . Only if the nitrogen was in the state corresponding to the transition being driven will a measurement of the  $m_s = 0$  state give a positive result.

By resetting and repeating this procedure until a positive result is measured the nitrogen-spin can be initialized. The electronic spin-state can be reset by applying a resonant laser as shown in the previous section. The nuclear spin-state can be reset by applying two resonant lasers resonant with  $E_x$  and  $E'$ .

This procedure is known as measurement based initialization (MBI) and is used in our experiments. The lower panel of Fig. 2.2 shows an ESR after the nitrogen has been initialized using MBI.

### 2.2.3 Hyperfine coupling of carbon-13 spins

For carbon-13 spins the hyperfine term ( $H_{HF}$ ) of Eq. (2.4) consists of a contact term and a dipole term. The contact term results from an overlap between the electronic- and nuclear- wave-functions. The contact term is negligible for all but the carbon-spins closest to the NV-center. For close-by carbon spins hyperfine couplings have been calculated [11, 12] and measured [24].

For carbons where the contact term is negligible the dipole term is dominant and is given by Eq. (2.7) [6]:

$$H_{\text{dip}} = \frac{\mu_0 \gamma_e \gamma_C \hbar^2}{4\pi r^3} [\mathbf{S} \cdot \mathbf{I} - 3(\mathbf{S} \cdot \hat{\mathbf{n}}_{\text{HF}})(\mathbf{I} \cdot \hat{\mathbf{n}}_{\text{HF}})] \quad (2.7)$$

Where  $\hat{n}_{\text{HF}}$  is a unit vector pointing from the electronic spin to the nucleus,  $r$  is the distance between the electronic and nuclear spin, and  $\mu_0$  the magnetic constant. The dipole term can be split into a parallel and orthogonal component such that:

$$H_{\text{HF}} = A_{\parallel} I_z + A_{\perp} I_x \quad (2.8)$$

From Eq. (2.7) the parallel and orthogonal components of the hyperfine interaction, with respect to the NV-axis along the z-direction, can be derived to be:

$$A_{\parallel} = -\frac{\mu_0 \gamma_e \gamma_C \hbar^2}{4\pi r^3} \left( 3 \cdot \frac{z^2}{r^2} - 1 \right) \quad (2.9)$$

$$A_{\perp} = -\frac{\mu_0 \gamma_e \gamma_C \hbar^2}{4\pi r^3} \left( 3 \cdot \frac{\sqrt{x^2 + y^2} \cdot z}{r^2} \right) \quad (2.10)$$

### 2.2.4 Strongly coupled spins

Carbon spins can be controlled using the methods described in Section 2.2.2 when it is possible to selectively address its spin-dependent transitions. When two transitions can be resolved in an ESR they can be addressed by applying microwave pulses of the corresponding frequencies. However if two transitions overlap in an ESR, applying a microwave pulse at the corresponding frequency will address both transitions.

Two transitions cannot be resolved when the splitting between them is smaller than the width of the transition. The magnitude of the splitting is determined by the strength of the interaction and the broadening of the transitions is caused by decoherence. We define a spin to be strongly coupled when it is possible to readily resolve its transitions in an ESR experiment with negligible power broadening. Conversely a spin is weakly coupled when it is not possible to readily resolve its transitions in an ESR.

Using the methods described in Section 2.2.2 strongly-coupled carbon-13 spins have been controlled and initialized [21].

The next section will explain what decoherence is and how it relates to the broadening of transitions. The next chapter will discuss how spins for which transitions cannot be resolved can be addressed through dynamical decoupling.

## 2.3 Decoherence

The ESR signal is broadened because the NV-center interacts with the spin bath in its environment. The spin bath consists of spins that are coupled to the NV-center. Just like the uninitialized nitrogen spin these are in a mixed state. This means that for every iteration of an experiment the spin bath can have a different configuration. These different configurations of the spin bath slightly shift the addressed electron transition causing the broadening of the transition.

### 2.3.1 Decoherence time

The variations in the spin-bath configuration can be measured with a Ramsey experiment. In a Ramsey experiment (Fig. 2.3a) the electronic spin is brought into a superposition between the  $|0\rangle$  and  $|1\rangle$ -state where it freely evolves for a time  $\tau$ . Provided the coherent superposition is preserved, a final pulse brings the state back into  $|0\rangle$  where it is read out.

By applying a slight detuning to the rotating frame used to keep the phase fixed an oscillation can be seen in the signal (Fig. 2.3b). Due to the different spin-bath configurations the evolution frequency varies slightly between experiments, this causes the measured signal to decay as the different oscillations move out of phase with each other. The decay is known as decoherence and the  $1/e$ -time of the decay is known as the decoherence time  $T_2^*$ . For a Ramsey experiment the decay follows a Gaussian profile Eq. (2.11):

$$K(\tau) = e^{-(\frac{\tau}{T_2^*})^n} \quad (2.11)$$

Where  $K$  is the amplitude and  $n = 2$  for a Gaussian profile. The  $T_2^*$  of the NV-electron spin used in this thesis was measured to be  $T_{2,e}^* = 4.54 \pm 14 \mu\text{s}$  with initialized nitrogen-spin. The decay follows a Gaussian profile within two  $\sigma$ :  $n = 1.81 \pm 0.14$ .

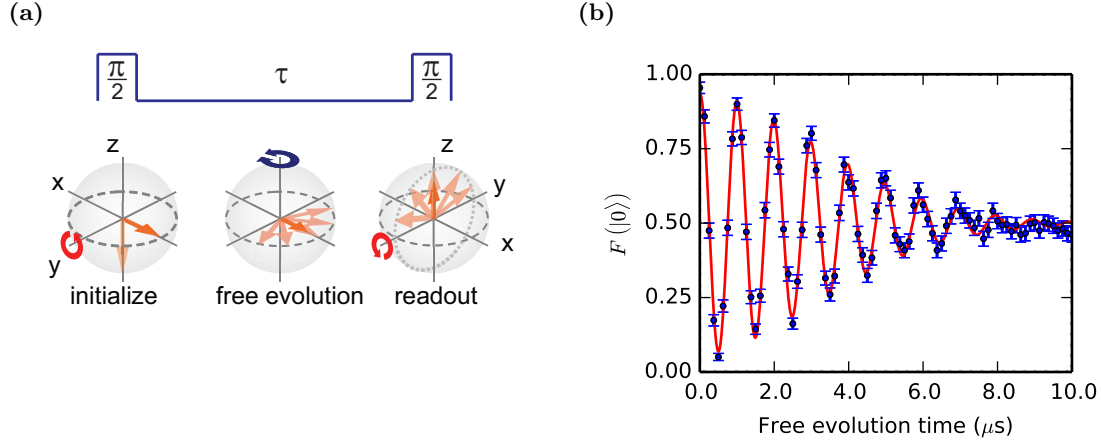


**Figure 2.3** – (a) schematic representation of a Ramsey experiment. Figure from de Lange [6]. In a Ramsey experiment a qubit is brought into the  $xy$ -plane by a  $\pi/2$ -pulse where it evolves freely for a time  $\tau$  before being subjected to a final  $\pi/2$  pulse to read out its  $x$ -component. By applying a detuning ( $\omega_d$ ) to the rotating frame the spin will pick up a phase  $\phi = \omega_d\tau$  during free evolution. The final pulse will rotate the spin towards the poles depending on the phase picked up during free evolution. This manifests itself as an oscillation. Because the configuration of the spin-bath is slightly different between experiments the frequency of the oscillation will vary with each iteration. This variation in frequency between iterations will cause the oscillation to decay. (b) shows a Ramsey experiment for the electronic spin. The  $y$ -axis shows the fidelity of the measured state to the  $|0\rangle$ -state of the electronic spin. A  $T_{2e}^*$  of  $4.54 \pm 0.14 \mu\text{s}$  was measured for the electronic spin. The decay follows a Gaussian profile within uncertainty  $n = 1.81 \pm 0.14$ .

### 2.3.2 Relation between decoherence and transition broadening

The decay in a Ramsey experiment is a measure for variations of the spin-bath in the time-domain while the broadening of transitions in an ESR is a measure for variations of the spin-bath in the frequency domain. The decay of the Ramsey and the shape of the ESR for negligible power broadening are related through a Fourier transform and described by Eq. (2.12) :

$$\mathcal{F}\{K(\tau)\} = Ce^{-\frac{(2\pi \cdot f)^2 \cdot T_{2e}^{*2}}{4}} \quad (2.12)$$

Where  $C$  is a normalization constant. Because the decay of the Ramsey is Gaussian the shape of a transition in the ESR is also Gaussian.

Two identical Gaussians can be readily resolved when the separation between their maxima is larger than their full-width-half-maximum (FWHM). The FWHM (in Hz) of the ESR is given by Eq. (2.13):

$$\text{FWHM} = \frac{2\sqrt{\ln 2}}{\pi T_{2e}^{*}} \quad (2.13)$$

An estimation of when carbon spins can be resolved is given by the strength of the hyperfine interaction. At low magnetic field ( $\gamma_e B \ll A$ ) the splitting caused by a carbon spin is equal to the total interaction strength  $A$ . At high field ( $\gamma_e B \gg A$ ) the secular approximation is valid and the splitting is equal to the parallel component of the hyperfine  $A_{||}$ . We can readily resolve a transition when the shift due to the corresponding interaction is larger than the FWHM of the transition.

At a natural concentration of carbon-13 spins ( $\mu = 1.1\%$ ) NV-centers have a typical electron  $T_{2e}^* \approx 2 \mu\text{s}$  at low field that depends on the exact configuration of the spin-environment. Increasing the carbon-13 concentration generally reduces  $T_{2e}^*$ . On the sample used for the experiments  $T_{2e}^* = 4.54 \pm 0.14 \mu\text{s}$  was measured at 304 G. This means that the hyperfine coupling must be larger than  $2\pi \cdot 265 \text{ kHz}$  in a typical NV-center, and larger than  $2\pi \cdot 117 \text{ kHz}$  in the sample used in this thesis for a carbon to be strongly coupled.

As the presence of strongly coupled carbons close to the NV-center is governed by probability and the probability of getting 3-5 strongly coupled carbons is very low it is necessary to develop methods to address weakly coupled carbons. The next chapter will demonstrate methods to extend the coherence time and address weakly coupled carbons, thereby enlarging the spin-register.



# 3

## Addressing Weakly-coupled Carbon Spins

In order to realize quantum error correction we need at least three qubits and at least five to correct for a universal error. Figure 3.1 shows a schematic overview of spins in different coupling regimes. Strongly coupled carbon spins can be controlled using the methods described in the previous chapter. However the probability of finding enough of these spins to implement QEC is very small. The probability of finding three or more strongly coupled carbons spins in an NV-center is low and goes down the more carbons are required [26, 29]. Additionally strongly coupled nuclear spins are prone to decohere when the electronic spin is optically addressed. A problematic feature for QEC which relies on repeatedly measuring errors to be able to correct for them.

By addressing weakly coupled carbon spins the spin register can be enlarged with spins that are not affected as strongly by the readout of the electron spin. However to address weakly coupled carbon spins the coherence of the electron needs to be extended. This is done through dynamical decoupling [7]. Van der Sar et al. [27] have demonstrated how to integrate regular operations on the NV-spin with a dynamical decoupling sequence. To address these weakly coupled carbon spins we use the dynamical decoupling sequence used to extend the coherence [25]. In the next chapter it is demonstrated how this control is used to perform parity measurements and create entanglement.

In this chapter it will first be explained how the coherence can be extended through dynamical decoupling so that weakly coupled carbon spins can be addressed. The dynamical decoupling sequence will then be used to identify spins in the environment. These spins are characterized so that they can be controlled in the next chapter.

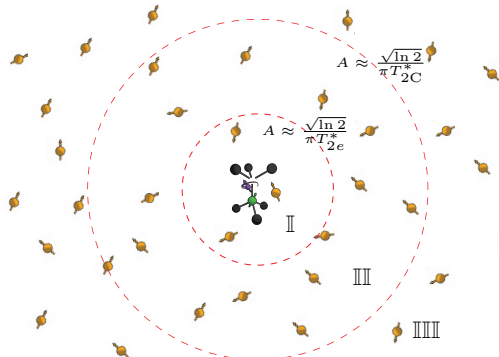


**Figure 3.1** – Schematic representation of different coupling regimes. Carbons in region II are in the strong coupling regime, transitions of these spins can be readily resolved and they can be controlled using the methods described in the previous chapter. In the weak coupling regime (region III) carbon-spins are coupled more strongly to the NV-center than to the spin-bath but not strong enough to be readily resolvable in an ESR. These spins can be controlled through dynamical decoupling [25]. In the very-weak coupling regime (region IIII) the coupling to the spin-bath is stronger than the coupling to the NV-center. These spins cannot presently be addressed.

## 3.1 Extending Electron Coherence

To be able to resolve weakly coupled carbons it is necessary to extend the coherence of the NV-spin. By using a technique known as a spin-echo the effect of variations in the environment *between experiments* can be eliminated, making dynamics *during* experiments the main source of decoherence. By dynamical decoupling the effect of these dynamics on the coherence can be minimized and the dynamics of the spin-bath can be exposed.

### 3.1.1 Spin-Echo

A spin echo experiment (Fig. 3.2) is very similar to a Ramsey experiment. The difference is an additional  $\pi$  pulse that is added in the middle of the experiment exactly between the  $\pi/2$  pulses of the Ramsey sequence. In a spin echo the state is brought into the  $xy$ -plane where it evolves for a time  $\tau/2$  before a  $\pi$ -pulse, along the  $y$ -direction in the rotating frame, is applied. It evolves for another  $\tau/2$  before a final  $\pi/2$ -pulse rotates it back towards  $|0\rangle$  and it is read out.

The key component of a spin-echo is the central  $\pi$ -pulse that cancels out the effect of quasi-static variations in the spin-bath configuration. The  $\pi$ -pulse can be seen as turning the reference frame of the NV-spin upside down. If the spin-bath configuration is approximately static during the sequence, the detuning of the evolution frequency with respect to the central frequency during the first part will be exactly opposite to the detuning during the second part. This means that any phase difference picked up during the first half of the evolution is canceled out during the second half of the evolution.

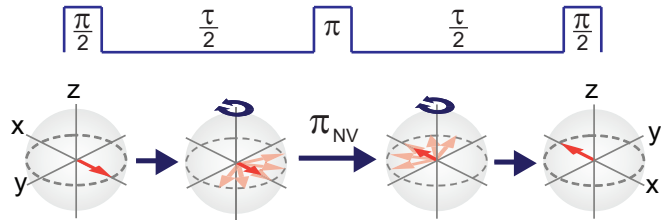


**Figure 3.2** – In a spin echo experiment the qubit is brought into the  $xy$ -plane of the Bloch-sphere by a  $\pi/2$ -pulse. Here it freely evolves for a time  $\tau/2$  before being flipped by a  $\pi$ -pulse along the  $y$ -axis of the rotating frame. It is let to evolve for another  $\tau/2$  before a final  $\pi/2$  pulse brings it to read out the  $x$ -component. If the spin-bath configuration does not change during the free evolution time  $\tau$  the state vector will end up along the  $x$ -axis irrespective of the initial spin-bath configuration. Figure from de Lange [6].

Because the spin-bath does not remain static during experiments the cancellation is not perfect, some phase is picked up causing the signal to decohere. This coherence time ( $T_2$ ) is defined as the  $1/e$  value of the decay of a spin echo experiment and measures decoherence due to dynamics in the spin-bath during an experiment.  $T_2$  was measured to be  $1.10 \pm 0.01$  ms.

### 3.1.2 Dynamical Decoupling

A natural way to extend the phase cancellation properties of the spin-echo experiment to shorter timescales is by applying more  $\pi$ -pulses. This procedure is known as dynamical decoupling. Similar to how the spin-echo cancels out phase picked up due to any variations that are quasi-static on the time-scale of the experiment, dynamical decoupling cancels out phase due to variations on the time-scale of the  $\pi$ -pulses. Dynamical decoupling can significantly improve coherence times [7].

On the NV-center used in this thesis a coherent signal<sup>1</sup> is measured after more than 40 ms for 256 pulses. Work on ensembles indicates that this can be improved even further by applying more pulses: a coherence time of  $T_{DD} \approx 0.6$  s was reported at 77 K [1].

### 3.1.3 Dynamical decoupling spectroscopy

When discussing the Ramsey and the spin-echo experiment we have treated the NV-center as being affected by the spin-bath but not affecting it. In reality the interaction works both ways and the NV-spin does affect the nuclear spins. It is possible to probe these interactions using a dynamical

<sup>1</sup> $F|0\rangle > 0.68$

decoupling spectroscopy. A dynamical decoupling spectroscopy provides a type of fingerprint of the nuclear spin environment from which the hyperfine interaction for the individual spins can be determined.

In a dynamical decoupling spectroscopy experiment the electron is prepared in the  $|X\rangle = \frac{1}{\sqrt{2}}(|0\rangle + |1\rangle)$  state. It is subjected to a pulse sequence consisting of  $N/2$  blocks of the form  $\tau - \pi - 2\tau - \pi - \tau$ , where  $\tau$  is a wait time and  $\pi$  a  $\pi$ -pulse. The experiment is concluded by measuring  $\langle X \rangle$ . The fingerprint is the result of many repetitions for a range of inter-pulse delays  $2\tau$ .

Part of a dynamical decoupling spectroscopy result can be seen in Fig. 3.3. When the electron spin performs an entangling operation on a spin in the environment coherence is lost when the electron spin is measured. In a dynamical decoupling spectroscopy such an interaction is visible as a lowered contrast. The physical processes resulting in such a fingerprint will be discussed in the next section.

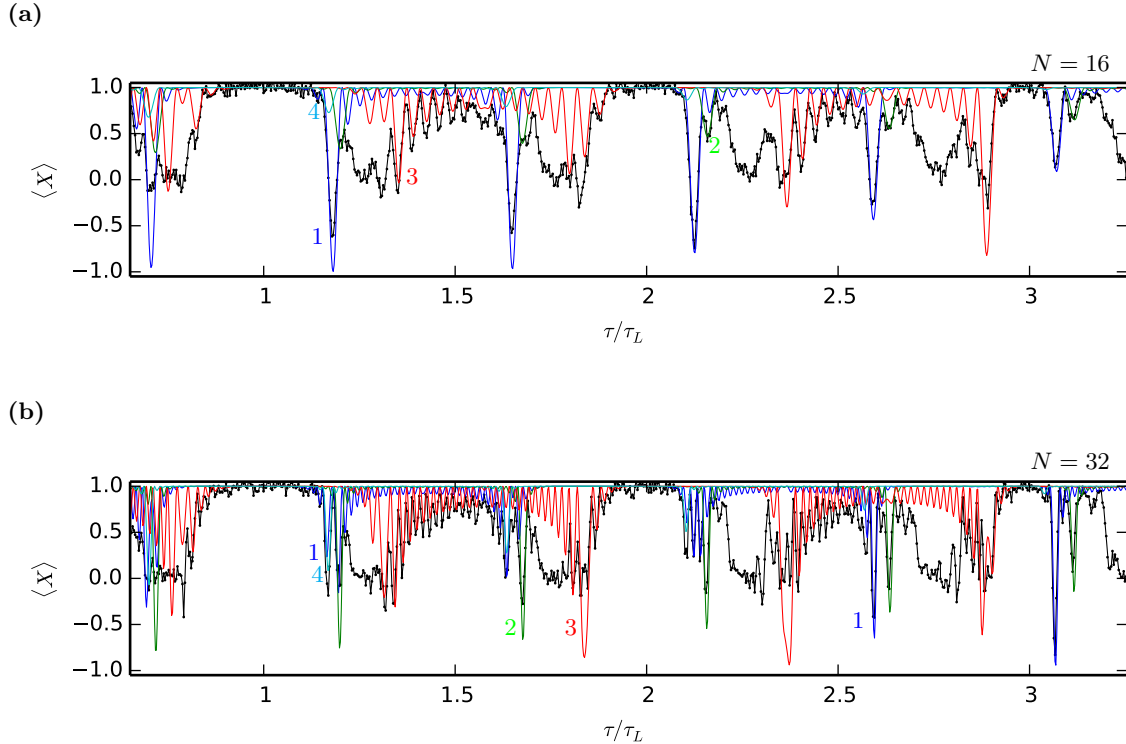


**Figure 3.3** – Part of a dynamical decoupling spectroscopy experiment performed at  $B_z = 304$  G,  $\tau_L = 3.07 \mu\text{s}$ . Black lines correspond to data. Colored lines represent computed responses of carbon spins. (a)  $N = 16$  pulses; (b)  $N = 32$  pulses. Contrast is lowered when the decoupling sequence performs an entangling operation on a spin in the environment. A reference to the full dynamical decoupling dataset can be found in Appendix A.2. Responses were calculated using Eq. (A.2) with hyperfine parameters from Table 3.1.

## 3.2 Identifying weakly-coupled carbon-pins

This section will discuss the effect of dynamical decoupling on the interaction between the NV-center and weakly coupled nuclear spins. This is used to explain the features in the fingerprint of Fig. 3.3 and identify several nuclear spins.

### 3.2.1 The effect of dynamical decoupling on nuclear spins

During dynamical decoupling the electronic state alternates between the  $m_s = 0$  and  $m_s = +1$  state, this causes the nuclear spin to alternately rotate around two distinct quantization axes (Fig. 3.4). When the electron is in the  $m_s = 0$  state each nuclear spin precesses about  $\omega_L$  with the Larmor frequency given by Eq. (2.5). When the electron is in the  $m_s = +1$  state there is a hyperfine

interaction between the nucleus and the NV-center (Eq. (2.4)) and the spin precesses around  $\tilde{\omega} = \omega_L + \mathbf{A}$ , where  $\mathbf{A} = A_{\parallel}\hat{z} + A_{\perp}\hat{x}$  [25].

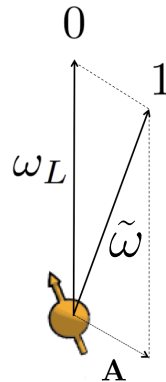


**Figure 3.4** – Flipping the electron spin from the  $m_s = 0$  to the  $m_s = +1$  state changes the quantization axis of nuclear spins. For  $m_s = 0$  all nuclear spins precess about  $\omega_L$ . For  $m_s = +1$  each spin precesses about a distinct axis  $\tilde{\omega} = \omega_L + \mathbf{A}$  due to the hyperfine interaction.

The result of a decoupling sequence is a net rotation around an axis  $\hat{n}_i$  by an angle  $\theta$ . Where  $\hat{n}_i$  depends on the initial state of the electron and  $\theta$  is proportional to the number of pulses  $N$  [25].  $\hat{n}_i = \hat{n}_0$  when the electron starts in  $m_s = 0$  and  $\hat{n}_i = \hat{n}_1$  when the electron starts in  $m_s = +1$ .

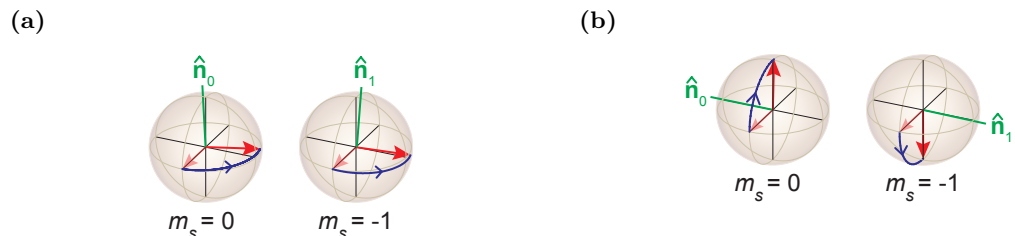


**Figure 3.5** – (a) When the net rotation axes  $\hat{n}_0$  and  $\hat{n}_1$  point in the same direction the carbon experiences an unconditional rotation. (b) When the net rotation axes  $\hat{n}_0$  and  $\hat{n}_1$  are anti-parallel the carbon experiences a conditional rotation, either around  $+x$  or  $-x$ . Figure from Taminiau et al. [25].

When the net rotation axes point in a different direction a conditional operation is executed during dynamical decoupling (Fig. 3.5). In a dynamical decoupling spectroscopy contrast is lowered when a conditional operation is executed. To understand when this occurs it is useful to consider three different cases. A weakly coupled carbon spin in: the trivial regime where  $A_{\perp} = 0$ , the basic regime where  $A_{\perp} \ll \omega_L$  and the complex regime where  $A_{\perp} \sim \omega_L$ . For a mathematical description of the result of a dynamical decoupling spectroscopy the reader is referred to Appendix A.1.

### The trivial regime ( $A_{\perp} = 0$ )

Because there is no orthogonal component of the hyperfine the spin will precess around the  $z$ -axis independent of the initial electronic spin-state. Therefore the operation not conditional and no signal for such spins is observed in a dynamical decoupling spectroscopy.

### The basic regime ( $A_{\perp} \ll \omega_L$ )

In the basic regime the net rotation axes are practically parallel and point in the  $z$ -direction for almost every  $\tau$  except for a specific resonant condition for which the axes are anti-parallel. This resonant condition is given by Eq. (3.1):

$$\tau = \frac{(2k+1)\pi}{2\omega_L + A_{\parallel}} \quad (3.1)$$

Where  $k$  is an integer, and has a Lorentzian shape in a dynamical decoupling spectroscopy. These sharp resonances are the origin of the sharp dips in the dynamical decoupling spectroscopy. The FWHM of the resonance is given by Eq. (3.2):

$$\text{FWHM}_{\text{DD}} = \frac{A_{\perp}}{2\omega_L^2} \quad (3.2)$$

### The complex regime ( $A_{\perp} \sim \omega_L$ )

In the case where  $\omega_L$  and  $A_{\perp}$  are of comparable magnitude the net rotation axes are strongly dependent on the initial electron-state for almost any  $\tau$ . When a carbon is in this regime it is no longer possible to describe it as a narrow resonance in the dynamical decoupling spectroscopy. The response is visible as a wide resonance with an oscillation on top of it, spin 3 in Fig. 3.3 is an example of such a spin.

When the response of multiple carbon spins in a dynamical decoupling spectroscopy overlaps, the electron performs an entangling operation on all these carbons. Because of this the measured contrast in a dynamical decoupling spectroscopy goes down rapidly when the responses of multiple carbons overlap. This makes it hard to resolve individual spins when a spin has a broad response, such as a spin in the complex regime, or if there are several spins with similar hyperfine couplings.

#### 3.2.2 Identifying Individual Carbon-spins

Using the previous section we will look at Fig. 3.3 in greater detail.

A broad collapse of the signal is clearly visible around  $\tau/(4\tau_L) = m$  for odd  $m$ . This broad collapse is caused by the response of multiple spins overlapping.

At the edges of this collapse several sharp dips are visible. These correspond to individual spins. A first estimate of the hyperfine coupling to these spins can be made based on their location and width using Eqs. (3.1) and (3.2).

Between the broad collapses there alternately appears an oscillation. This oscillation is caused by a spin in the complex regime. Its position can be used to get a rough estimate for its hyperfine coupling.

By computing the responses for the hyperfine parameters using Eq. (A.2) a more accurate estimation was made. 13 distinct carbon spins were identified.

The parameters of the 4 strongest coupled carbons are listed in Table 3.1 and their computed responses are visible as colored lines in Fig. 3.3. All estimated hyperfine parameters and a link to the full dynamical decoupling dataset can be found in Appendix A.2.

**Table 3.1** – Estimated hyperfine parameters for spins 1 to 4 in Fig. 3.3.

Carbon	$A_{\parallel}$	$A_{\perp}$
1	$2\pi \cdot 30.0$ kHz	$2\pi \cdot 80.0$ kHz
2	$2\pi \cdot 27.0$ kHz	$2\pi \cdot 28.5$ kHz
3	$2\pi \cdot -51.0$ kHz	$2\pi \cdot 105.0$ kHz
4	$2\pi \cdot 45.1$ kHz	$2\pi \cdot 20.0$ kHz

### 3.3 Characterizing weakly-coupled carbon spins

Using the knowledge of the interaction between the NV-center and individual nuclear spins it is possible to implement basic gates and characterize the spins. This section will first explain how basic gates can be implemented on weakly coupled carbon spins. These gates are then used to measure the precession frequency and  $T_2^*$  for individual carbon spins.

#### 3.3.1 Basic operations

In order to implement basic gates on a nuclear spin we make use of the conditional rotation that occurs on the resonance given by Eq. (3.1). At the resonant condition the nuclear spin rotates about one of two anti-parallel axes depending on the electronic-spin state. The angle of the rotation is proportional to the number of pulses on the electron ( $N$ ). By sweeping the number of pulses to perform a  $\pi/2$  rotation a maximally entangling gate is performed. We define the axis of rotation of this operation as the  $x$ -axis and call the operation the  $\pm x$ -gate.

By bringing the electron in a superposition, sweeping the number of pulses on the electron and measuring the contrast an oscillation can be measured. This oscillation can be used to calibrate the  $\pm x$ -gate. For twice the number of pulses ( $N_{\pm x}$ ) required to implement the  $\pm x$ -gate the contrast is -1 for an ideal  $\pm x$ -gate. The fidelity with which the oscillation can be swept to -1 is equal to the squared fidelity with which the  $\pm x$ -gate can be implemented.

The  $\pm x$ -gate forms the basis of our control over weakly coupled spins. Figure 3.6 shows how the  $\pm x$ -gate is depicted in a circuit-diagram. A non entangling rotation can be implemented by placing the electron in an eigenstate before performing the  $\pm x$ -operation. By letting the phase of the carbon evolve we are able to apply operations on the carbon-spin with arbitrary phase.

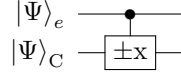


**Figure 3.6** – The  $\pm x$ -gate performs an  $x$ -rotation on the carbon ( $|\Psi\rangle_C$ ) when the electron is in the  $|0\rangle_e$ -state. It performs a  $-x$ -rotation when the electron is in the  $|1\rangle_e$ -state.

The  $\pm x$ -gate has been calibrated for several spins. The parameters used to implement  $\pm x$ -gates are listed in Table 3.2. Of these carbon-1 and carbon-4 were selected for the experiments.

**Table 3.2** – Parameters used to implement  $\pm x$ -gates.

Carbon	$N$	$\tau$	total gate time
1	18	9.420 $\mu\text{s}$	339 $\mu\text{s}$
2	26	6.620 $\mu\text{s}$	344 $\mu\text{s}$
3	14	18.564 $\mu\text{s}$	520 $\mu\text{s}$
4	40	6.456 $\mu\text{s}$	516 $\mu\text{s}$

### 3.3.2 Carbon Ramsey experiment

By performing a Ramsey experiment the precession and dephasing-time  $T_2^*$  can be determined. The precession frequencies are required to calculate the phase required to implement operations with the correct phase. By measuring the precession frequency it is also possible to test our estimation for the hyperfine parameters.

In an ordinary Ramsey experiment a qubit is brought to the equator of the Bloch-sphere where it precesses for a time  $\tau$  before it is read out along the  $x$ -direction. A carbon-Ramsey experiment is similar.

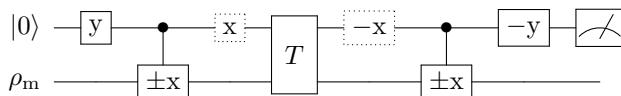


**Figure 3.7** – Gate circuit depicting an uninitialized carbon Ramsey.  $T$  is the free evolution time.  $x$  and  $y$  are  $\pi/2$  pulses along the  $x$  and  $y$  axis respectively. The dotted gates are not present when the electron is protected against decoherence by dynamical decoupling during the free evolution time  $T$ .

The gate circuit of the uninitialized carbon-Ramsey experiment is depicted in Fig. 3.7. The first pulse brings the electronic spin in the  $|X\rangle$ -state. Because the carbon starts out in a mixed state the two-qubit system can be described by the tensor product of two density matrices:

$$\rho_X \otimes \rho_m = \rho_X \otimes \rho_X + \rho_X \otimes \rho_{-X} \quad (3.3)$$

By applying the  $\pm x$ -gate the electronic-spin picks up a phase depending on the nuclear spin-state:

$$\rho_Y \otimes \rho_X + \rho_{-Y} \otimes \rho_{-X} \quad (3.4)$$

In this state it is either left to freely evolve for a time  $T$  while the electronic spin is protected against decoherence through dynamical decoupling, or a  $\pi/2$ -pulse is applied to bring the electron back to the poles of the Bloch-sphere. If the extra  $\pi/2$ -pulse is applied the system is in the following state before the free evolution.

$$\rho_0 \otimes \rho_X + \rho_1 \otimes \rho_{-X} \quad (3.5)$$

Because the electronic spin is in a different state for  $\rho_X$  and  $\rho_{-X}$  they evolve with different frequencies. After the free evolution another  $\pi/2$ -pulse is applied to bring the electronic spin back into the  $xy$ -plane.

The final part of the circuit reads out the nuclear spin along the  $x$ -direction for  $|Y\rangle_e$  and along the  $-x$ -direction for  $|-Y\rangle_e$ . The phase picked up during free evolution shows up as an oscillation between  $|0\rangle_e$  and  $|1\rangle_e$  in the readout.

## Determining the precession frequency

Because the uninitialized carbon-Ramsey evolves with two frequencies we expect the measured oscillation to be the sum of two cosines as described by Eq. (3.6):

$$c_1 - c_2 \cos(\omega_L \tau) - c_3 \cos(\tilde{\omega} \tau) \quad (3.6)$$

Where  $\tilde{\omega} = \sqrt{(\omega_L + A_{\parallel})^2 + A_{\perp}^2}$  and  $c_1$ ,  $c_2$  and  $c_3$  are constants.

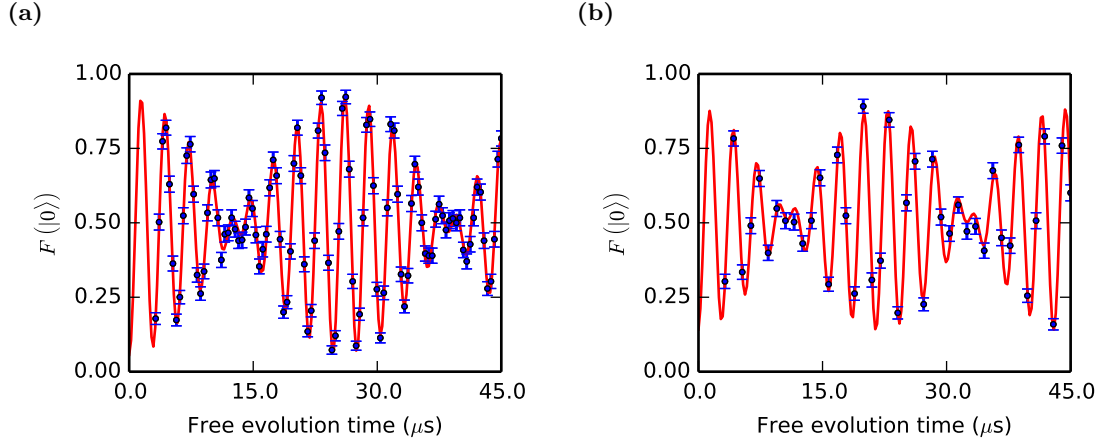


**Figure 3.8** – The uninitialized carbon-Ramsey experiment shows an oscillation due to the phase picked up during free evolution. (a) shows data for carbon-1 and (b) for carbon-4. The measured frequencies were, for carbon-1:  $\omega_{L,C1} = 2\pi \cdot 325.81 \pm 0.25$  kHz for carbon-1 and  $\tilde{\omega}_{C1} = 2\pi \cdot 364.41 \pm 0.23$ , and for carbon-4:  $\omega_{L,C4} = 2\pi \cdot 325.94 \pm 0.40$  and  $\tilde{\omega}_{C4} = 2\pi \cdot 371.52 \pm 0.39$ .

Figure 3.8 shows the results for an uninitialized carbon-Ramsey experiment. The data was fitted to a sum of two cosines in order to determine the frequencies.

The Larmor frequencies measured are  $\omega_{L,C1} = 2\pi \cdot 325.81 \pm 0.25$  kHz for carbon-1 and  $\omega_{L,C4} = 2\pi \cdot 325.94 \pm 0.40$  kHz for carbon-4. Both the measured Larmor frequencies agree with the magnetic field of 304 G within two standard deviations.

Based on the estimated hyperfine parameters we expect  $\tilde{\omega}_{C1} \approx 2\pi \cdot 364.7$  kHz for carbon-1 and  $\tilde{\omega}_{C4} \approx 2\pi \cdot 371.4$  kHz for carbon-4. For carbon-1  $\tilde{\omega}_{C1} = 2\pi \cdot 364.41 \pm 0.23$  kHz was measured and for carbon-4  $\tilde{\omega}_{C4} = 2\pi \cdot 371.52 \pm 0.39$  kHz was measured. Both these values are in good agreement with experiment, an indication that our hyperfine estimation is accurate.

## Measuring $T_{2,C}^*$

To determine  $T_{2,C}^*$  for normal operation an uninitialized carbon-Ramsey was performed where the electron was dynamically decoupled during the free evolution time. Dynamical decoupling was performed at  $\tau = 8 \cdot \tau_L$  by varying the number of pulses  $N$ .  $\tau_L$  is the Larmor period  $1/\omega_L$  of the carbon. Because the electron is constantly flipped the carbon will precess with an average frequency of  $\omega_{DD} = (\omega_L + \tilde{\omega})/2$ . By undersampling with a frequency slightly detuned from the precession frequency ( $\omega_{DD}$ ) a decaying cosine can be observed where the  $1/e$  time of the envelope is equal to  $T_2^*$ . Because this decaying cosine can be measured for a relatively long time ( $\sim$  ms) this method can also be used to accurately determine the precession frequency.

Figure 3.9 shows the decay for both carbons. The decay follows a Gaussian profile within uncertainty for both spins. The coherence times measured were  $T_{2,C1}^* = 9.85 \pm 0.39$  ms for carbon-1 and  $T_{2,C4}^* = 6.68 \pm 0.22$  ms for carbon-4. It should be noted that these  $T_2^*$  values are not limited by the electron coherence which was measured to be larger than 40 ms for  $N = 256$  pulses.

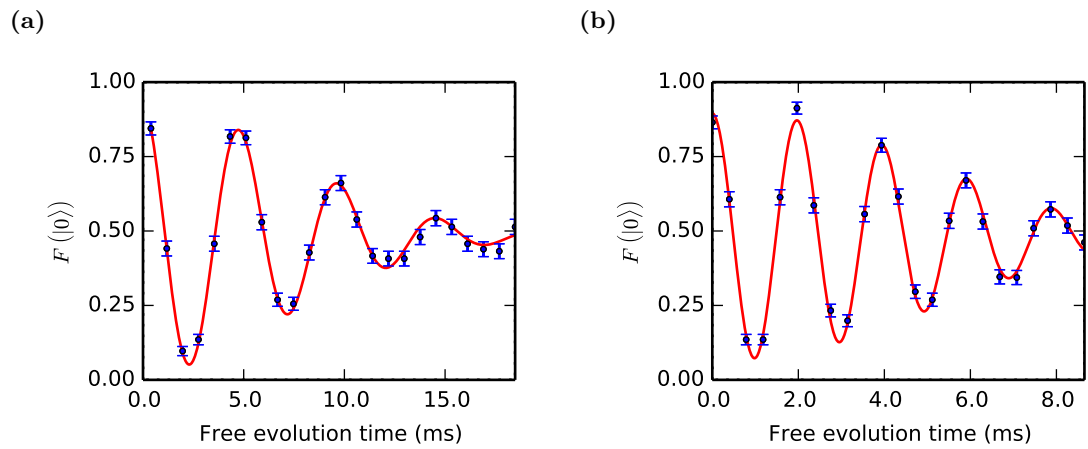


**Figure 3.9** – Carbon-Ramsey experiment to determine  $T_2^*$  for nuclei while decoupling the electron. Dynamical decoupling during evolution is implemented at  $8\cdot\tau_L$  of the carbon spin. Free evolution time is varied by varying the number of pulses. The decays are fitted with a generalized normal distribution to determine  $T_2^*$  and the exponent  $n$ . (a) Ramsey decay for carbon-1,  $T_{2,C1}^* = 9.85 \pm 0.39$  ms and  $n = 1.83 \pm 0.19$ . (b) Ramsey decay for carbon-4,  $T_{2,C4}^* = 6.68 \pm 0.22$  ms and  $n = 2.31 \pm 0.31$ .

# 4

## Entangling Weakly-coupled Carbon Spins

The creation of entanglement is an essential capability for QEC in particular and quantum-computation in general. This chapter demonstrates how weakly coupled carbon spins can be initialized and read-out and how this is used to generate entanglement between two weakly coupled carbon spins.

### 4.1 Initialization and readout of single spins

A weakly coupled spin can be initialized by conditioning on a measurement result, similar to how the nitrogen initialization works (Section 2.2.2). A weakly coupled carbon spin can be measured by entangling the phase of the electronic-spin with the state of the carbon spin and reading out the phase of the electronic spin.

The gates used to initialize a weakly coupled carbon are depicted in Fig. 4.1. The circuit depicted in Fig. 4.1a projects the carbon spin along the the  $x$ -axis upon readout of the electronic spin. By adding an additional conditional gate, as depicted in Fig. 4.1b, the carbon spin is brought into the  $|0\rangle$ -state regardless of the measurement outcome of the electronic spin.

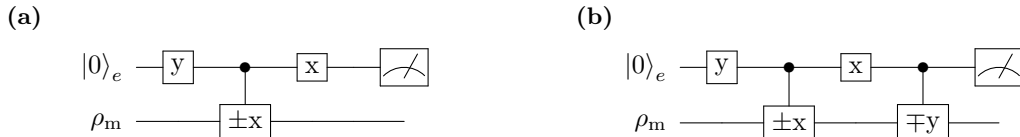


**Figure 4.1** – (a) MBI-based initialization into  $\pm|X\rangle$ . Initializes the carbon into  $|X\rangle_C$  when  $|0\rangle_e$  is measured and into  $|-X\rangle_C$  when  $|1\rangle_e$  is measured for the electron. (b) MBI-swap initialization into  $|0\rangle$ . Initializes the carbon into  $|0\rangle_C$  regardless of the electronic spin-state measured.

To initialize the carbon spin an initial pulse brings the electronic spin in  $|X\rangle_e$ . When the carbon spin starts in the mixed state the system can be described by the tensor product of two density matrices:

$$\rho_X \otimes \rho_m = \rho_X \otimes \rho_X + \rho_X \otimes \rho_{-X} \quad (4.1)$$

By applying the  $\pm x$ -gate the electronic-spin picks up a phase depending on the carbon spin-state:

$$\rho_Y \otimes \rho_X + \rho_{-Y} \otimes \rho_{-X} \quad (4.2)$$

By reading out the electronic spin along the  $y$ -axis the carbon spin is projected into the  $|X\rangle_C$  or  $|-X\rangle_C$ -state. This correlates the electronic-spin readout to the  $x$ -projection of the carbon spin. By conditioning on a positive readout result the state can be initialized into the  $|X\rangle_C$ -state. By applying an additional  $\mp y$  gate the carbon spin can be initialized into  $|0\rangle$ .

A weakly coupled carbon spin can be read out along the  $x$ -direction using the same circuit as used to initialize into  $|X\rangle$ . By changing the conditional gate to  $\pm y$  the carbon can be read out along  $y$ . In order to read out the carbon along the  $z$ -direction an additional  $\pm z$ -gate is added before the initial  $y$ -pulse (Section 4.1). It should be noted that the  $z$ -readout does not leave the carbon spin in  $|0\rangle$  or  $|1\rangle$  but in  $|X\rangle$  or  $|-X\rangle$ .

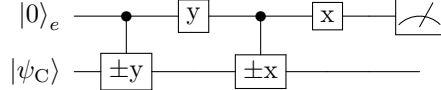


**Figure 4.2** – Gate circuit used to read out a carbon spin along  $z$ . The initial  $\pm y$  rotates the state onto the  $x$ -basis. The rest of the circuit is identical to the circuit in Fig. 4.1a and is used to read out the carbon spin along  $x$ .

Figure 4.3 demonstrates experimental initialization and readout of a carbon spin. In Fig. 4.3a carbon-1 is initialized into the  $|X\rangle_C$ -state and in Fig. 4.3b it is initialized into the  $|0\rangle_C$ -state. This is done by implementing the circuits depicted in Fig. 4.1 and conditioning on a positive electron readout result.

The blue points correspond to  $x$ -readout, the green points to  $y$ -readout and the red-points to the  $z$ -readout. The phase is swept to demonstrate that the readouts function as intended. For a qubit in the  $|0\rangle$ -state the initial phase is undefined.

The combined fidelity of readout and initialization to the desired state is:  $F(|X\rangle) = 90.57 \pm 0.85\%$  for the  $|X\rangle$ -state and  $F(|Z\rangle) = 93.00 \pm 0.31\%$  for the  $|Z\rangle$ -state.

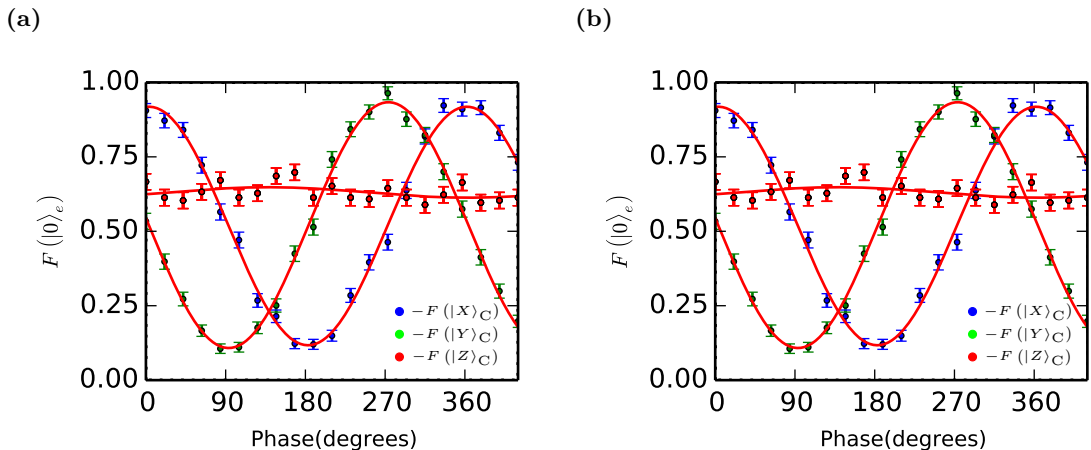


**Figure 4.3** – Demonstration of carbon initialization and readout. In (a) carbon-1 is initialized in  $|X\rangle$ . In (b) carbon-1 is initialized in  $|0\rangle$ . Colored points correspond to readouts in different bases, blue to  $x$ -readout, green to  $y$ -readout and red to  $z$ -readout. The red lines are fits to the data with a cosine:  $a + A \cos(\omega\phi + \phi_0)$ .

## 4.2 Parity measurements

Entanglement between two qubits can be created by performing a parity measurement on them and conditioning on the outcome.

A parity measurement measures if two qubits are the same in a certain basis. An example is the XX-parity measurement. The XX-parity measurement returns a positive result if the two qubits are parallel along  $x$  and a negative result if the two are anti-parallel. That is it returns a positive result if the state is a linear combination of  $|X, X\rangle$  and  $|-, -\rangle$  and a negative result if the state is a linear combination  $|X, -\rangle$  or  $|-, X\rangle$ . In general a two qubit parity operator has 2 eigenvalues, both are twofold degenerate.

The XX-parity measurement can be implemented on a weakly coupled carbon spins using the circuit depicted in Fig. 4.4. A parity measurement is similar to the regular readout depicted in Fig. 4.1a. Once the electron is brought into a superposition the electron picks up a phase when the  $\pm x$ -gate is applied:  $+\pi/2$ -phase when the carbon is in  $|+X\rangle$  and  $-\pi/2$ -phase when the carbon is in  $|-, -\rangle$ . This is done for both carbons, when both carbons are in the same  $x$ -state the electron will pick up  $\pi$ -phase. When they do not give the same result the phase cancels. By reading out the electronic-spin along  $x$  the parity is measured. It should be noted that because we use a  $\pm x$ -gate instead of a CNOT-gate an additional  $\pi/2$ -phase is added to the carbon states. For the odd parity measurements considered in the experiments this is of no concern as the phase cancels out.

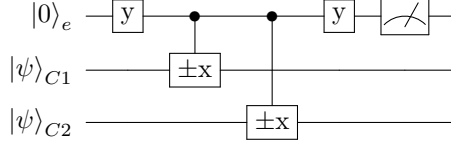


Figure 4.4 – Gate circuit for a XX-parity measurement.

### 4.3 Quantum state tomography

In this thesis the entangled state is verified by performing a quantum state tomography. In a quantum state tomography the density matrix of a quantum state is reconstructed by repeatedly preparing the same state and gathering measurement statistics in different bases.

An arbitrary density matrix can be described as a weighted sum of the Pauli-matrices and the Identity Eq. (4.3):

$$\rho = \frac{1}{4} \sum_{i,j} a_{i,j} \sigma_i \otimes \sigma_j, \quad \text{for } \sigma_i, \sigma_j \in \{I, X, Y, Z\} \quad (4.3)$$

By measuring the coefficients  $a_{i,j}$  which correspond to experimental values the density matrix  $\rho$  can be reconstructed completely.

#### 4.3.1 Readout

To measure the required experimental values single and multi qubit measurements are needed. Single qubit measurements were described in Section 4.1. The two qubit measurements required are very similar to parity measurements but do not necessarily need to preserve the state after the measurement.

The parity measurement depicted in Fig. 4.4 is used to measure the XX-parity. By changing the phase of one of the two  $\pm x$  gates a Y-parity can be measured. By applying a  $\mp y$  to one of the two carbons before the initial  $y$ -pulse a Z-parity can be measured. As an example Fig. 4.5 implements the YZ-parity measurement.

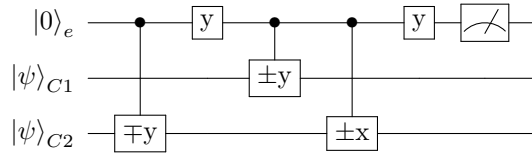


Figure 4.5 – Example of a parity measurement that measures the YZ-parity.

#### 4.3.2 Initialization and tomography of multiple weakly coupled spins

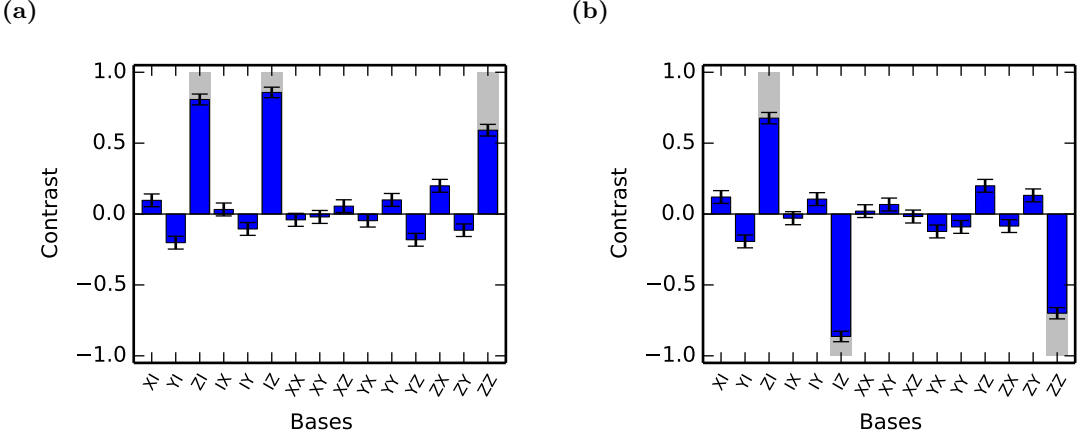
The tomography is performed on two initialized two-qubit states. The combined fidelity of the initialization and tomography is calculated by comparing to the ideal case.

Figure 4.6a shows a tomography of carbon-1 and carbon-4 initialized in the  $|00\rangle$ -state. In the ideal case the single qubit Z-measurements and the ZZ parity are 1 and all other coefficients are 0. The ideal case is represented by the gray bars in the Fig. 4.6a. The fidelity to the ideal case is  $F = 81.43 \pm 1.68 \%$ .

Figure 4.6b shows a tomography of carbon-1 and carbon-4 initialized in the  $|01\rangle$ -state. In the ideal case ZI = 1 and IZ and ZZ are -1, all other coefficients are 0. The ideal case is represented by the gray bars in the Fig. 4.6b. The fidelity to the ideal case prediction is  $80.99 \pm 1.69 \%$ .

### 4.4 Demonstrating entanglement between weakly coupled carbons

We combine multi-qubit initialization, parity measurements and the quantum state tomography to demonstrate entanglement. After the qubits are initialized an XX-parity is performed and the tomography is conditioned on the negative electron readout result. The experiment is done for carbons initialized in  $|00\rangle$  and carbons initialized in  $|01\rangle$ .



**Figure 4.6** – Quantum state tomographies of two initialized carbons. In (a) the carbons are initialized into  $|00\rangle$  with a fidelity of  $81.43 \pm 1.68\%$ . In (b) the carbons are initialized into  $|10\rangle$  with a fidelity of  $80.99 \pm 1.69\%$ .

By conditioning on the negative readout result the carbons are projected into the negative-parity eigenspace of the XX-parity operator:  $|{-X}, X\rangle$  and  $|{-X}, X\rangle$ . Ideally the tomography correlation for the XX-parity is -1. The other coefficients depend on the initial state the parity was performed on.

Figure 4.7a shows the tomography for the negative XX parity of the  $|00\rangle$ -state.  $|00\rangle$  can be written in the  $x$ -basis as:

$$|00\rangle = \frac{1}{2} (|X, X\rangle + |X, -X\rangle + |-X, X\rangle + |-X, -X\rangle) \quad (4.4)$$

By measuring the negative XX-parity the state is projected onto:

$$\Psi = \frac{1}{\sqrt{2}} (|X, -X\rangle + |-X, X\rangle) \quad (4.5)$$

In the  $y$ -basis this state can be written as:

$$\Psi = \frac{1}{\sqrt{2}} (|Y, Y\rangle + |-Y, -Y\rangle) \quad (4.6)$$

And in the  $z$ -basis this is:

$$\Psi = \frac{1}{\sqrt{2}} (|00\rangle - |11\rangle) \quad (4.7)$$

It follows that  $\langle YY \rangle = \langle ZZ \rangle = +1$ . The fidelity to the ideal case prediction is  $76.60 \pm 1.74\%$ .

Figure 4.7b shows the tomography for the negative XX parity of the  $|01\rangle$ -state.  $|01\rangle$  can be written in the  $X$ -basis as:

$$|01\rangle = \frac{1}{2} (|X, X\rangle - |X, -X\rangle + |-X, X\rangle - |-X, -X\rangle) \quad (4.8)$$

By measuring the negative XX-parity the state is projected onto:

$$\Phi = \frac{1}{\sqrt{2}} (|{-X}, X\rangle - |X, {-X}\rangle) \quad (4.9)$$

In the  $yy$ -basis this state can be written as:

$$\Phi = \frac{i}{\sqrt{2}} (|Y, -Y\rangle - |-Y, Y\rangle) \quad (4.10)$$

And in the  $zz$ -basis this is:

$$\Phi = \frac{1}{\sqrt{2}} (|10\rangle - |01\rangle) \quad (4.11)$$

It follows that  $\langle YY \rangle = \langle ZZ \rangle = -1$ . The fidelity to the ideal case prediction is  $76.08 \pm 1.74\%$

Both measured parities show a fidelity to respective Bell-state well above 0.5, demonstrating that the states are entangled and that the parity measurement is successfully implemented.

we have successfully created an entangled state between weakly coupled carbon-spins.

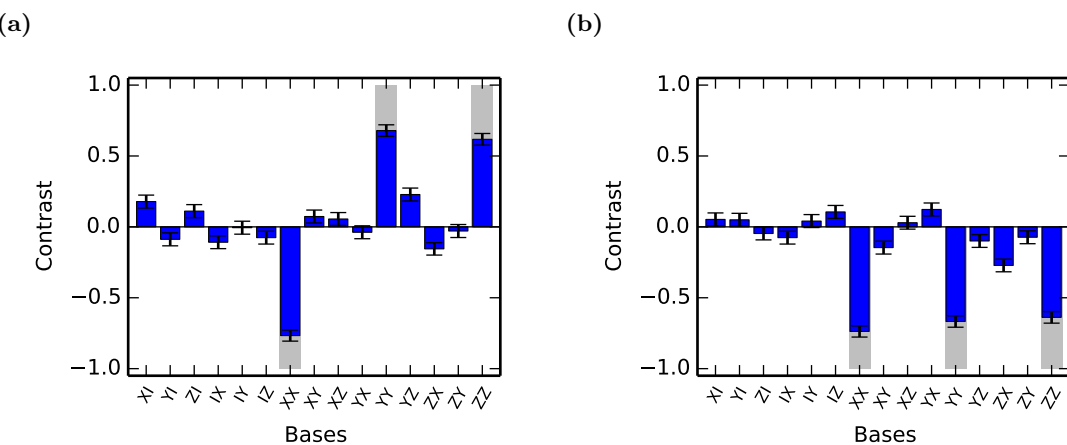


**Figure 4.7** – Quantum state tomographies for entangled states created by measuring a negative XX parity. (a) is the negative XX-parity of the state prepared in (a). It is projected into  $\frac{1}{\sqrt{2}}(|X, -X\rangle + |X, -X\rangle)$  with  $76.60 \pm 1.74\%$  fidelity. (b) is the negative XX-parity of the state prepared in (b). It is projected into  $\frac{1}{\sqrt{2}}(|X, -X\rangle - |X, -X\rangle)$  with  $76.08 \pm 1.74\%$  fidelity.



# 5

## Towards Quantum Error Correction

Two more challenges remain to realize quantum error correction based on the parity measurements demonstrated in Chapter 4. First, to correct errors, gate operations that are conditional on the parity outcome are required. Therefore the parity measurement must be accurate and preserve entangled state for both outcomes, unlike the probabilistic initialization and entanglement in this thesis.

Second, for error correction encoding in larger entangled states is required: at least three qubits for the simplest error correction and at least five qubits for correction of all types of errors. In this chapter I address these two challenges and present simulations that indicate that multi-qubit parity measurements on weakly coupled spins are possible.

### 5.1 Deterministic Parity Measurements

An essential capability for QEC is the ability to perform different quantum operations based on a classical readout result. An example of such an experiment is the deterministic creation of entanglement, as was demonstrated by Rist et al. [20] in a different system.

By applying an extra set of gates when the negative result is measured in a parity measurement the state can be transformed in the state that would have been created had the positive parity been measured. This capability is particular important for QEC where the result of a parity measurement determines whether a correcting gate must be applied.

The main challenge when performing such operations is to keep track of the phase of the system while waiting for the readout result that determines which set of gates should be executed. The measurement environment developed for the work in this thesis automatically keep track of phases and has been set up to be extendable and compatible with such feed forward capabilities.

### 5.2 Multi Qubit Control

In order to implement QEC more than the two qubits that were addressed must be addressed. To correct for a single type of quantum error 3 qubits are required. To correct for any type of quantum error at least 5 qubits are required.

#### 5.2.1 Working of the simulations

Simulations were performed to determine how many weakly coupled carbons can be controlled, on average, for an NV-center using dynamical decoupling. In the simulations statistics were collected on 1000 NV-centers for a range of magnetic fields and three different carbon-13 concentrations. For all NV-centers an environment of carbon-13 spins randomly placed on lattice points was generated. For lower concentrations a larger environment was simulated such that the total number of simulated carbon spins was  $\sim 300$  per NV-center for all concentrations.

NV-centers containing a carbon with a hyperfine coupling larger than 200 kHz were rejected as such spins are prone to decohere during the optical readout of the electron spin and their complex dynamics at moderate field complicate spin control of other spins (Chapter 3). In an experimental setting these carbons can be easily detected and the NV-centers rejected.

On the remaining centers the hyperfine coupling between each carbon and the NV-center as well as the resonance conditions of these carbons were calculated. At these resonances it was determined if a carbon can be selectively and coherently controlled.

As a figure of merit we take the fidelity  $F$  of the electron spin after two consecutive  $\pm x$  gates. The first gate entangles the electron spin with the nuclear spin and the second gate disentangles the two. Reduced electron spin fidelity indicates gate imperfections or unwanted entanglement of the electron to the other carbon-13 spins. The threshold for a carbon-13 to be considered controllable is set at  $F = 90\%$ .

The fidelity is determined by sweeping the number of pulses at the resonance conditions and determining with what fidelity two consecutive  $\pm x$ -gates can be implemented. The accuracy with which the resonance can be addressed is limited by the resolution of the arbitrary waveform generator at 1 ns. The fidelity is determined under the assumption of perfect  $\pi$  and  $\pi/2$  pulses on the electron.

Additionally we require to be able to perform 10 such gates within the coherence time. For simplicity we do not simulate the nuclear-nuclear interactions and instead set  $T_2^*$  as in Table 5.1. Finally, we set a maximum value for the inter pulse delay  $\tau_{\max}$ , to take into account the limited coherence for the electron at large  $\tau$ .  $\tau_{\max}$  is set at the values listed in Table 5.1.

**Table 5.1** – Coherence times and maximum resonance time as used in the simulations.

Concentration	$T_{2,C}^*$	$\tau_{\max}$
1.10 %	7ms	10 $\mu$ s
0.33 %	45ms	36.7 $\mu$ s
0.11 %	70ms	100 $\mu$ s

### 5.2.2 Results of the simulation

Figure 5.1a shows the average number of addressable carbon spins as a function of magnetic field. The number of addressable carbons increases quickly at first before a slow decay sets in.

The initial increase in the number of addressable carbons can be explained by the Larmor frequency becoming larger than the hyperfine interaction. At low magnetic field ( $\omega_L \sim A$ ) most spins undergo complex dynamics. When the Larmor frequency becomes larger than the hyperfine coupling of a carbon spin it is in the simple regime where the resonances are narrow. Because there is less overlap more spins can be addressed. This increase drops off because eventually all spins are in the simple regime.

By increasing the magnetic field further the resonances both get narrower (Eq. (3.2)) and move to shorter times Eq. (3.1). When the field becomes too high a resonance can become too narrow to accurately address. This is limited by the 1ns timing resolution of the arbitrary waveform generator. Therefore the number of addressable spins decreases at high fields.

For lower concentrations there are on average less spins undergoing complex dynamics for the same magnetic field. This causes the initial increase in addressable carbons to be steeper at lower concentrations.

There is also a bias due to the rejection of carbons with  $|A| > 200$  kHz. Not rejecting these carbons will lower the number of addressable carbons for low magnetic fields as the response of these carbons dominates the dynamical decoupling spectroscopy, while the number of addressable carbons will increase slightly in the high field limit were these carbons can be controlled through dynamical decoupling.

Figure 5.1b shows the distribution of addressable carbons for a natural concentration of carbon-13 at the magnetic field that has the highest average number of addressable carbons. It indicates that in most NV-centers (89 %) three or more carbons can be addressed and that in a reasonable fraction (57 %) of the samples five or more carbons can be addressed. There are even rare occurrences where ten or more carbons can be addressed.

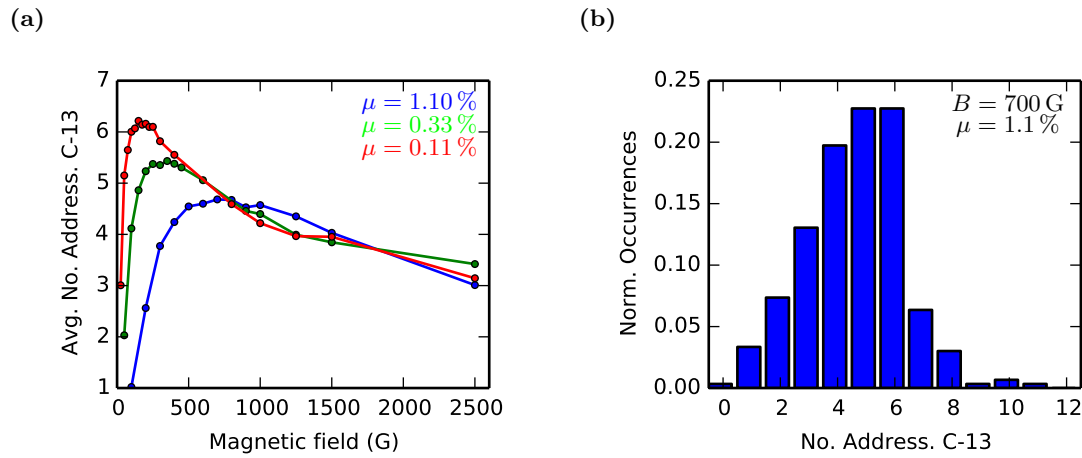


**Figure 5.1** – Simulation results calculating the number of addressable carbons in NV-centers containing no carbons with hyperfine coupling larger than 200kHz. (a) Average number of addressable carbons at different concentrations. (b) Normalized occurrences for  $\mu = 1.1\%$  at 700 G. The simulation indicates that an NV-center likely has 3 or more addressable carbons( $P = 89\%$ ), that there is a good chance that 5 or more carbons can be addressed ( $P = 57\%$ ) and that there is even a small probability of getting  $\sim 10$  addressable carbon spins.



## Bibliography

- [1] N Bar-Gill, L M Pham, A Jarmola, D Budker, and R L Walsworth. Solid-state electronic spin coherence time approaching one second. *Nature communications*, 4:1743, 1 2013. ISSN 2041-1723. URL <http://www.ncbi.nlm.nih.gov/pubmed/23612284>.
- [2] H. Bernien. *Control, Measurement and Entanglement of Remote Quantum Spin Registers in Diamond*. PhD thesis, Delft University of Technology, 2014.
- [3] H. Bernien, B. Hensen, W. Pfaff, G. Koolstra, M. S. Blok, L. Robledo, T. H. Taminiau, M. Markham, D. J. Twitchen, L. Childress, and R. Hanson. Heralded entanglement between solid-state qubits separated by three metres. *Nature*, 497(7447):86–90, 5 2013. ISSN 1476-4687. URL <http://www.ncbi.nlm.nih.gov/pubmed/23615617>.
- [4] L. Childress and R. Hanson. Diamond nv centers for quantum computing and quantum networks. *MRS Bulletin*, 38(02):134–138, 2 2013. ISSN 0883-7694. URL [http://www.journals.cambridge.org/abstract\\_S0883769413000201](http://www.journals.cambridge.org/abstract_S0883769413000201).
- [5] D. Cory, M. Price, W. Maas, E. Knill, R. Laflamme, W. Zurek, T. Havel, and S. Somaroo. Experimental quantum error correction. *Physical Review Letters*, 81(10):2152–2155, 9 1998. ISSN 0031-9007. URL <http://link.aps.org/doi/10.1103/PhysRevLett.81.2152>.
- [6] G. de Lange. *Quantum Control and Coherence of Interacting Spins in Diamond*. PhD thesis, Delft University of Technology, 2012.
- [7] G. de Lange, Z.H. Wang, D. Rist, V.V. Dobrovitski, and R. Hanson. Universal dynamical decoupling of a single solid-state spin from a spin bath. *Science (New York, N.Y.)*, 330(6000):60–3, 10 2010. ISSN 1095-9203. URL <http://www.ncbi.nlm.nih.gov/pubmed/20829452>.
- [8] M.W. Doherty, N.B. Manson, P. Delaney, F. Jelezko, J. Wrachtrup, and L.C.L. Hollenberg. The nitrogen-vacancy colour centre in diamond. page 101, 2 2013. URL <http://arxiv.org/abs/1302.3288>.
- [9] Richard P. Feynman. Simulating physics with computers. *International Journal of Theoretical Physics*, 21(6-7):467–488, 6 1982. ISSN 0020-7748. URL <http://link.springer.com/10.1007/BF02650179>.
- [10] Austin G. Fowler, Matteo Mariantoni, John M. Martinis, and Andrew N. Cleland. Surface codes: Towards practical large-scale quantum computation. *Physical Review A*, 86(3):032324, 9 2012. ISSN 1050-2947. URL <http://link.aps.org/doi/10.1103/PhysRevA.86.032324>.
- [11] Adam Gali. Identification of individual extasciicircum{13}c isotopes of nitrogen-vacancy center in diamond by combining the polarization studies of nuclear spins and first-principles calculations. *Physical Review B*, 80(24):241204, 12 2009. ISSN 1098-0121. URL <http://link.aps.org/doi/10.1103/PhysRevB.80.241204>.
- [12] Adam Gali, Maria Fyta, and Efthimios Kaxiras. Ab initio supercell calculations on nitrogen-vacancy center in diamond: Electronic structure and hyperfine tensors. *Physical Review B*, 77

- (15):155206, 4 2008. ISSN 1098-0121. URL <http://link.aps.org/doi/10.1103/PhysRevB.77.155206>.
- [13] Bas Jorrit Hensen. *Measurement-based Quantum Computation with the Nitrogen-Vacancy centre in Diamond*. PhD thesis, Delft University of Technology, 2011.
  - [14] F. Jelezko, T. Gaebel, I. Popa, a. Gruber, and J. Wrachtrup. Observation of coherent oscillations in a single electron spin. *Physical Review Letters*, 92(7):076401, 2 2004. ISSN 0031-9007. URL <http://link.aps.org/doi/10.1103/PhysRevLett.92.076401>.
  - [15] N David Mermin. Extreme quantum entanglement in a superposition of macroscopically distinct states. *Physical Review Letters*, 65(15):1838–1840, 10 1990. ISSN 0031-9007. URL <http://link.aps.org/doi/10.1103/PhysRevLett.65.1838>.
  - [16] O. Moussa, J. Baugh, C. A. Ryan, and R. Laflamme. Demonstration of sufficient control for two rounds of quantum error correction in a solid state ensemble quantum information processor. *Physical Review Letters*, 107(16):160501, 10 2011. ISSN 0031-9007. URL <http://link.aps.org/doi/10.1103/PhysRevLett.107.160501>.
  - [17] M.A. Nielsen and I.L. Chuang. *Quantum Computation and Quantum Information*. Cambridge University Press, 2010.
  - [18] W. Pfaff, B. Hensen, H. Bernien, S. B. van Dam, M. S. Blok, T. H. Taminiau, M. J. Tiggelman, R. N. Schouten, M. Markham, D. J. Twitchen, and R. Hanson. Unconditional quantum teleportation between distant solid-state quantum bits. *Science*, 532, 5 2014. ISSN 0036-8075. URL <http://www.sciencemag.org/cgi/doi/10.1126/science.1253512>.
  - [19] M D Reed, L DiCarlo, S E Nigg, L Sun, L Frunzio, S M Girvin, and R J Schoelkopf. Realization of three-qubit quantum error correction with superconducting circuits. *Nature*, 482(7385):382–5, 2 2012. ISSN 1476-4687. URL <http://www.ncbi.nlm.nih.gov/pubmed/22297844>.
  - [20] D Rist, M Dukalski, C a Watson, G de Lange, M J Tiggelman, Ya M Blanter, K W Lehnert, R N Schouten, and L DiCarlo. Deterministic entanglement of superconducting qubits by parity measurement and feedback. *Nature*, 502(7471):350–4, 10 2013. ISSN 1476-4687. URL <http://www.ncbi.nlm.nih.gov/pubmed/24132292>.
  - [21] L. Robledo, L. Childress, H. Bernien, B. Hensen, P.F.A. Alkemade, and R. Hanson. High-fidelity projective read-out of a solid-state spin quantum register. *Nature*, 477(7366):574–8, 9 2011. ISSN 1476-4687. URL <http://www.ncbi.nlm.nih.gov/pubmed/21937989>.
  - [22] P. Schindler, J.T. Barreiro, T. Monz, V. Nebendahl, D. Nigg, M. Chwalla, M. Hennrich, and R. Blatt. Experimental repetitive quantum error correction. *Science (New York, N.Y.)*, 332(6033):1059–61, 5 2011. ISSN 1095-9203. URL <http://www.ncbi.nlm.nih.gov/pubmed/21617070>.
  - [23] P.W. Shor. Algorithms for quantum computation: discrete logarithms and factoring. In *Proceedings 35th Annual Symposium on Foundations of Computer Science*, pages 124–134. IEEE Comput. Soc. Press, 1994. ISBN 0-8186-6580-7. URL <http://ieeexplore.ieee.org/lpdocs/epic03/wrapper.htm?arnumber=365700>.
  - [24] Benjamin Smeltzer, Lilian Childress, and Adam Gali. 13 c hyperfine interactions in the nitrogen-vacancy centre in diamond. *New Journal of Physics*, 13(2):025021, 2 2011. ISSN 1367-2630. URL <http://stacks.iop.org/1367-2630/13/i=2/a=025021?key=crossref.bdd6956722cde89a36ab3eee44a82724>.
  - [25] T. H. Taminiau, J.J.T. Wagenaar, T. van der Sar, F. Jelezko, V.V. Dobrovitski, and R. Hanson. Detection and control of individual nuclear spins using a weakly coupled electron spin. *Physical Review Letters*, 109(13):137602, 9 2012. ISSN 0031-9007. URL <http://link.aps.org/doi/10.1103/PhysRevLett.109.137602><http://arxiv.org/abs/1205.4128>.
  - [26] T. H. Taminiau, J. Cramer, T. van der Sar, V. V. Dobrovitski, and R. Hanson. Universal control and error correction in multi-qubit spin registers in diamond. *Nature Nanotechnology*, 2(February):2–7, 9 2014. ISSN 1748-3387. URL <http://arxiv.org/abs/1309.5452><http://www.nature.com/doifinder/10.1038/nnano.2014.2>.

- [27] T. van der Sar, Z.H. Wang, M.S. Blok, H. Bernien, T.H. Taminiau, D.M. Toyli, D.A. Lidar, D.D. Awschalom, R. Hanson, and V.V. Dobrovitski. Decoherence-protected quantum gates for a hybrid solid-state spin register. *Nature*, 484(7392):82–6, 4 2012. ISSN 1476-4687. URL <http://www.ncbi.nlm.nih.gov/pubmed/22481361>.
- [28] L M Vandersypen, Matthias Steffen, Gregory Breyta, Costantino S Yannoni, Mark H Sherwood, and Isaac L Chuang. Experimental realization of shor’s quantum factoring algorithm using nuclear magnetic resonance. *Nature*, 414(6866):883–7, 2001. ISSN 0028-0836. URL <http://www.ncbi.nlm.nih.gov/pubmed/11780055>.
- [29] G Waldherr, Y Wang, S Zaiser, M. Jamali, T. Schulte-Herbrggen, H. Abe, T. Ohshima, J. Isoya, J. F. Du, P. Neumann, and J. Wrachtrup. Quantum error correction in a solid-state hybrid spin register. *Nature*, 1 2014. ISSN 0028-0836. URL <http://arxiv.org/abs/1309.6424><http://www.nature.com/doifinder/10.1038/nature12919>.



# A

## Dynamical Decoupling Spectroscopy

### A.1 Mathematical description of dynamical decoupling spectroscopy

The observed signal due to the interaction between the NV-center and a single carbon in a dynamical decoupling spectroscopy experiment is given by Eqs. (A.1) to (A.4) [25]. Where  $P_x$  is the probability that the initial spin-state is preserved and  $M_j$  the contrast.

$$P_x = (M + 1)/2 \quad (\text{A.1})$$

$$M_j = 1 - (1 - \hat{\mathbf{n}}_0 \cdot \hat{\mathbf{n}}_1) \sin^2 \frac{N\phi}{2} \quad (\text{A.2})$$

$$1 - \hat{\mathbf{n}}_0 \cdot \hat{\mathbf{n}}_1 = \frac{A_\perp^2}{\tilde{\omega}^2} \frac{(1 - \cos(\tilde{\omega}\tau))(1 - \cos(\omega_L\tau))}{1 + \cos(\tilde{\omega}\tau)\cos(\omega_L\tau) - \left(\frac{A_\parallel + \omega_L}{\tilde{\omega}}\right) \sin(\tilde{\omega}\tau)\sin(\omega_L\tau)} \quad (\text{A.3})$$

$$\phi = \cos^{-1} \left( \cos(\tilde{\omega}\tau)\cos(\omega_L\tau) - \left(\frac{A_\parallel + \omega_L}{\tilde{\omega}}\right) \sin(\tilde{\omega}\tau)\sin(\omega_L\tau) \right) \quad (\text{A.4})$$

The contrast due to an ensemble of spins in a dynamical decoupling spectroscopy  $M$  is given by the product of all individual values  $M_j$  for each individual spin  $j$  (Eq. (A.5)).

$$M = \prod_j M_j \quad (\text{A.5})$$

### A.2 Fingerprint analysis

The estimated hyperfine parameters of all 13 identified spins can be found in Table A.1. Due to the size of the fingerprint analysis it is not possible to include with this thesis. A pdf file containing the fingerprint analysis can be found here: <https://www.dropbox.com/s/gieji9e86bfvsf1/fingerprinting.pdf>.

**Table A.1** – Estimated hyperfine parameters for spins 1 to 13.

Carbon	$A_{\parallel}$	$A_{\perp}$
1	$2\pi \cdot 30.0$ kHz	$2\pi \cdot 80.0$ kHz
2	$2\pi \cdot 27.0$ kHz	$2\pi \cdot 28.5$ kHz
3	$2\pi \cdot -51.0$ kHz	$2\pi \cdot 105.0$ kHz
4	$2\pi \cdot 45.1$ kHz	$2\pi \cdot 20.0$ kHz
5	$2\pi \cdot 17.0$ kHz	$2\pi \cdot 10.0$ kHz
6	$2\pi \cdot -15.0$ kHz	$2\pi \cdot 12.0$ kHz
7	$2\pi \cdot -23.0$ kHz	$2\pi \cdot 12.0$ kHz
8	$2\pi \cdot 10.0$ kHz	$2\pi \cdot 8.0$ kHz
9	$2\pi \cdot 8.0$ kHz	$2\pi \cdot 12.0$ kHz
10	$2\pi \cdot -9.3$ kHz	$2\pi \cdot 13.0$ kHz
11	$2\pi \cdot -10.0$ kHz	$2\pi \cdot 5.0$ kHz
12	$2\pi \cdot -30.0$ kHz	$2\pi \cdot 35.0$ kHz
13	$2\pi \cdot -32.0$ kHz	$2\pi \cdot 20.0$ kHz

# B

## Constants and Experimental values

Constants	
$\mu_0$	$4\pi \cdot 10^{-7} \frac{\text{V}\cdot\text{s}}{\text{A}\cdot\text{m}}$
Gyromagnetic Ratios	
$\gamma_e$	$2\pi \cdot 2.8025 \text{ MHz/G}$
$\gamma_N$	$2\pi \cdot 0.3077 \text{ kHz/G}$
$\gamma_C$	$2\pi \cdot 1.0705 \text{ kHz/G}$
Interaction Strengths	
$\Delta$	$2\pi \cdot 2.878 \text{ GHz}$
$Q$	$2\pi \cdot 4.946 \text{ MHz}$
$A_N$	$2\pi \cdot 2.186 \text{ MHz}$
Optics	
637 nm	471 THz



## **Acknowledgements**